

On the nature of Pb species in Pb-(over)exchanged zeolite: a combined experimental and theoretical study

Roos, D. P.; Scheinost, A.; Churakov, S. V.; Nagashima, M.; Cametti, G.;

Originally published:

September 2021

Microporous and Mesoporous Materials 327(2021), 111444

DOI: <https://doi.org/10.1016/j.micromeso.2021.111444>

Perma-Link to Publication Repository of HZDR:

<https://www.hzdr.de/publications/Publ-33007>

Release of the secondary publication
on the basis of the German Copyright Law § 38 Section 4.

CC BY-NC-ND

On the nature of Pb species in Pb-(over)exchanged zeolite: a combined experimental and theoretical study

Diana P. Roos^a, Andreas C. Scheinost^{b,c}, Sergey V. Churakov^{a,d}, Mariko Nagashima^e,
Georgia Cametti^{a*}

^a Institute of Geological Sciences, Baltzerstrasse 1+3, 3012 Bern, Switzerland

^b The Rossendorf Beamline at the European Synchrotron Radiation Facility (ESRF), Avenue des Martyrs 71, 38043 Grenoble, France

^c Helmholtz Zentrum Dresden Rossendorf, Institute of Resource Ecology, Bautzner Landstrasse 400, 01328 Dresden

^d Paul Scherrer Institut, Forschungstrasse 111, 5232 Villingen PSI, Switzerland

^e Graduate School of Sciences and Technology for Innovation, Yamaguchi University, Yamaguchi, 753-8512, Japan

*Corresponding Author:

Georgia Cametti

Email: georgia.cametti@geo.unibe.ch

Abstract

Structural properties of Pb-exchanged zeolites are of interest because of their applications in environmental remediation and in industrial processes. In this study, we report on a Pb-exchanged aluminosilicate zeolite (Pb-STI), with particular focus on the cationic species, which form inside the zeolitic pores as a result of the exchange experiments. The produced zeolite had chemical composition $\text{Pb}_{13.4}(\text{OH})_{10}\text{Al}_{17.4}\text{Si}_{54.6}\text{O}_{144} \cdot 38\text{H}_2\text{O}$, indicating a Pb^{2+} overexchange of approximately 50%. The **STI** framework maintained the *Fmmm* space group

characteristic of the type material. However, the extraframework occupants, Pb^{2+} , H_2O and OH^- , were characterized by a strong positional-disorder. The latter was resolved and interpreted combining Extended X-ray Absorption Fine Structure (EXAFS) analysis with Molecular Dynamics (MD) simulations. On average, Pb^{2+} ions are coordinated by 2 OH^- and 1 H_2O at distances $< 2.5 \text{ \AA}$, whereas bonds to framework oxygen-atoms were found only at longer distances ($> 2.8 \text{ \AA}$). Pb^{2+} adopts mainly a sided distorted coordination, indicating a stereochemical activity of the lone pair electrons. The obtained results were compared with those of other mono-cationic forms of **STI** zeolites. Based on the analysis of the framework distortion experienced after the incorporation of different metal ions, considerations are drawn on the potential effect of Pb^{2+} on the thermal stability of **STI** framework type zeolites.

Keywords: XAFS, **STI**, XRD, Molecular Dynamics

Introduction

Cation exchange is undoubtedly one of the most exploited properties of natural and synthetic zeolites. The ability to exchange the extraframework (EF) cation content with different cationic species has been widely applied not only for the removal of contaminated substances from water and soils [1,2] but also to produce zeolite structures with tailored features [3,4,5]. Indeed, the modification of the EF cation-content strongly affects the microporous properties, such as sorption, catalytic and dehydration behaviour that can significantly differ from those of the original untreated zeolite.

In the last decades, several studies focused on metal-exchanged zeolites with the aim of tuning and improving their performance for various applications. For instance, zeolites exchanged with Zn, Cu, Ag, Fe, Cd, were found to be highly efficient for catalytic [6,7,8], environmental-remediation [9,10] and selective-gas-sorption processes [3,4,11 and references herein]. Pb-exchanged zeolites have received special attention because of their importance in

environmental related problems (i.e. removal of Pb from wastewater and food) and their use in industrial processes [12]. Pb-modified mordenite is an efficient trap for volatile iodine species (I_2 and ICH_3) [13], and Pb-exchanged clinoptilolite can be used to remove Cr(VI) from aqueous solution [14]. Further, from a structural point of view, the case of Pb-zeolites is interesting due to the presence of different Pb-species or clusters that can form, under different exchange conditions, in the zeolitic cavities. For instance, Baekelant et al. [15] demonstrated that Pb clusters with high luminescence properties can be confined in Linde Type A (LTA) zeolite.

Many previous studies reported the so-called “overexchange process” of Pb [16-21]. Hereby, the zeolite structure retains more Pb species than those necessary to balance the negative charge of the aluminosilicate framework, if these species were all present as Pb^{2+} ions. This positive overcharge can be explained by the presence of $[Pb(OH)_x]^{(2-x)}$ species in addition to Pb^{2+} . The early work of Hertzenberg and Sherry [16] reported the overexchange of Pb in a Na-A zeolite when using a 0.1 M $Pb(NO_3)_2$ solution. Later, it was suggested that the extent of Pb-overexchange in zeolite-A increases with the pH of the solution [17]. Yeom and Seff [19] reported an overexchange of 5% and 50% in zeolite A when ion-exchanged in aqueous lead nitrate at pH = 4.3 and in aqueous lead acetate at pH = 6, respectively. Similarly, Pb-overexchange was observed also in Na-X zeolite [20, 21]. Several EF species can form, depending on the framework topology, Si/Al ratio, and eventual presence of other counter-cations. Since the nature of the EF cations, plays a fundamental role in the subsequent applications of the modified zeolite, a detailed investigation of their oxidation state, coordination chemistry and interaction with the framework is of paramount importance.

Stellerite is a medium microporous zeolite with **STI** framework type [22,23]. The topology has *Fmmm* symmetry and consists of two systems of interconnected channels. One, composed of 8-membered rings of tetrahedra (with channel dimensions 2.7×5.6 Å), runs parallel to [001]; the other is constituted by 10-membered rings of tetrahedra (with channel dimensions

4.7 × 5.0 Å) parallel to [100]. The crystal symmetry of this zeolite, and its dehydration behaviour, changes according to the type of cations, which occupy the zeolite pores [24-27]. Ca-stellerite, i.e. the natural occurring stellerite, has orthorhombic symmetry *Fmmm* [22,24] and ideal chemical composition $\text{Ca}_8\text{Al}_{16}\text{Si}_{56}\text{O}_{144} \cdot 58\text{H}_2\text{O}$. Ca atoms occupy the middle of the *t-sti-1** cavity [28] and are coordinated exclusively by H_2O . Recently, we characterized the fully exchanged Ag- and Cd-forms of stellerite [26-27]. A framework distortion was observed in both cases, with a symmetry reduction from the orthorhombic space group *Fmmm* to monoclinic *F2/m* (non-standard setting for *C2/m*). This distortion is accompanied by a change in the shape of the ten-membered ring channels, which became more elliptical compared to those in Ca-stellerite. Most important observation is that the dehydration behaviour of Ag- and Cd-stellerite followed a different path compared to that reported for the natural material, including the formation of new dehydrated phases at high temperatures and an overall reduction of the thermal stability.

In this study, we investigate the crystal structure of stellerite fully exchanged with Pb. The aim was to (i) determine eventual structural changes induced by the lead uptake; (ii) find out which Pb species are present in the structural voids; and (iii) compare the obtained data with those of the other cationic forms of stellerite. To have a complete and detailed picture of the structural features, we combined Single Crystal X-ray Diffraction (SC-XRD) with Molecular Dynamics (MD) simulations and X-ray Absorption Spectroscopy (XAS).

2. Experimental methods

2.1 Cation exchange experiment and chemical analyses

The sample used in this study was a natural stellerite from Gibelsbach, Fiesch (Valais Switzerland) with original chemical composition $\text{Ca}_{7.96}\text{K}_{0.83}\text{Na}_{0.33}(\text{Si}_{55.4}\text{Al}_{16.42})\text{O}_{144} \cdot 32\text{H}_2\text{O}$ [29]. This specimen was the same previously used in our studies on mono-cationic forms of

STI zeolites [25-27]. Small fragments of stellerite with dimension ranging from 0.1 to 1 mm were at first put in a Teflon autoclave filled with 2M NaCl solution for 4 weeks at 95(2)°C. The solution was renewed every three days. Subsequently, the obtained Na-exchanged crystals were let in contact with a 0.5M Pb(CH₃COO)₂ solution (pH =5,6) for additional 19 days at 95(2)°C. Also in this case the Pb(CH₃COO)₂ solution was renewed every three days. After the exchange experiments the crystals were washed with deionized water and qualitatively analyzed by energy dispersive spectrometry (EDS) using a scanning electron microscope (SEM). More accurate chemical data were obtained by electron microprobe analyses (EMPA) using a JEOL JXA-8230. The analytical conditions were: 15 kV, 2nA, beam diameter 10 µm, 10 s counting time. The following standard were used: K-feldspar for Si, Al, and K, hematite for Fe, MnO for Mn, periclase for Mg, wollastonite for Ca, SrBaNb₄O for Sr and Ba, PbVGe oxide for Pb. The crystal chemical formula of Pb-stellerite (Pb-STI) was computed on the basis of 72(Si+Al) atoms per formula unit.

2.2 Thermal analysis

Thermal gravimetric analysis (TGA) was performed using a Mettler Toledo TGA/SDTA 851. Pb-STI powder with an initial mass of 20.6380 mg was used for the analysis and placed into a 70 µL alox crucible. The experiment was carried out between 25 and 500 °C with a heating rate of 1 °C/min. The analysis was performed in a nitrogen atmosphere with a flow rate of 20 mL/min.

2.3 Single crystal X-ray diffraction (SC-XRD)

A fragment of Pb-STI with dimension 0.070 × 0.100 × 0.200 mm was glued on a glass fiber and mounted on a goniometer head. Diffraction data were collected with a Bruker APEX II diffractometer equipped with CCD area detector and a MoK α radiation (λ =0.71073 Å). High

redundant data (redundancy = 5), based on a monoclinic cell were collected to be able to discriminate between the *C*-centred monoclinic and *F*-centred orthorhombic space groups.

Data were integrated and corrected for absorption by using the software package Apex3 [30].

Structure solution was performed by direct methods using Shelxs [31] and final structural refinement was carried out by using neutral scattering atoms by Shelxl [32].

The analysis of the systematic lattice exceptions suggested an orthorhombic *F*-centred lattice and space group *Fmmm*. An alternative solution in the monoclinic space group *C2/m* was also tested to unravel eventual deviation from the orthorhombic symmetry [25]. Finally, the orthorhombic space group *Fmmm* was maintained (see results section). The atom labels of the framework were the same adopted for natural stellerite [25]. The extraframework occupants were located by difference Fourier maps.

Data collection parameters and data refinement details are reported in Table 1.

Corresponding cif file has been submitted as supplementary material. All structure drawings have been produced by VESTA [33].

2.4 Molecular dynamics (MD) simulations

The molecular dynamics simulations were performed in an isothermal-isobaric (NPT) ensemble with the software package CP2K, using the Gaussians and Plane Waves method [34]. The Perdew-Burke-Erzerhof functional was used to describe the electron exchange and correlations [35]. Kohn Sham orbitals were expanded using a linear combination of atom-centred Gaussian-type orbital functions. For each atom kind a short range double – ζ valence polarized basis set was used [36]. The integration step for equations of motion was 0.5 fs. The dispersion correction was taken into account employing DFT+D3 method [37].

The MD trajectories were simulated starting from two different structural models. The first one (PbSTI-12) consisted of a stellerite supercell $2 \times 1 \times 1$ containing 24 Pb, 372 O, 152 H, 112 Si, and 32 Al. This structural model corresponded to a 50% over-exchanged stellerite,

with chemical formula $\text{Pb}_{12} [\text{Al}_{16}\text{Si}_{56}\text{O}_{144}](\text{OH})_8 \cdot 34\text{H}_2\text{O}$. The starting coordinates of the framework were those of natural stellerite. Pb atoms were distributed in the *t-sti-I** cavity surrounded by H_2O . Hydroxyl groups were added to balance the surplus of positive charges due to the Pb-overexchange. A second structural model (PbSTI-12-2W) consisted of a stellerite supercell $2 \times 1 \times 1$ containing 24 Pb, 362O, 132 H, 112 Si, and 32 Al, corresponding to a Pb-STI with chemical composition $\text{Pb}_{12} [\text{Al}_{16}\text{Si}_{56}\text{O}_{144}](\text{OH})_8 \cdot 27\text{H}_2\text{O}$. This second model corresponds to an overexchanged Pb-STI with a lower water content (ca. 2 H_2O per Pb) compared to the previous one (PbSTI-12).

The data were collected from a 15 ps long MD trajectory of the PbSTI-12 model, after 10 ps pre-equilibration. Theoretical Extended X-ray Absorption Fine Structure (EXAFS) spectra were calculated using 158 consecutive MD snapshots separated by 100 fs interval. The FEFF 8.40 software [38,39] was used to obtain a spectrum for each Pb atom (i.e. 24 in total) in the supercell. Self-consistent calculation of the Fermi energies and scattering potential was performed by using a cluster radius of 4 Å. Multi scattering paths up to four legs with path length up to 8 Å were considered. The Debye-Waller and the amplitude reduction factor S_0^2 were set to 0.0002 Å² and 0.9, respectively. An energy shift correction of -5 eV was used according to the fittings of the experimental EXAFS. In total 24×158 spectra were averaged to obtain the theoretical EXAFS spectrum.

2.5 X-Ray Absorption Spectroscopy (XAFS)

Extended X-ray absorption fine-structure (EXAFS) spectra data were collected at the Rossendorf Beamline (ROBL) at the European Synchrotron Radiation Facility (ESRF) in Grenoble (France) [40]. A closed-cycle He cryostat (CryoVac GmbH, Germany) was used to measure the samples at 15 K to prevent photon-induced redox changes and to improve the signal quality by eliminating thermal/vibrational contributions to the Debye-Waller term. The spectra were measured in fluorescence mode at the Pb L₃-edge (13,035 eV) using an 18-

element Ge-detector (Mirion Technologies, Canberra) with FalconX8 (XIA) digital pulse processor. The X-ray beam was monochromatized by a Si(111) double-crystal monochromator, and higher harmonics were suppressed by two Rh-coated mirrors. XANES and EXAFS data analysis was performed with standard procedures using WinXAS [41], after energy calibration using a Pb foil. The threshold energy (E_0) was defined as the first inflexion point of the absorption edge, determined as knot of the second derivate of the absorption coefficient. Extraction of the EXAFS function was conducted by a cubic-spline fit from 2 to 10.2 \AA^{-1} using the auto-spline function of WinXAS to determine the optimum number of splines. The k^3 -weighted EXAFS function was then Fourier-transformed using a Bessel window with parameter 3 across the k -space from 2.0 to 10.2 \AA^{-1} . The theoretical phase shifts and backscattering amplitudes for shell fit were obtained with FEFF8.2 [42], using the DFT-optimized structure of Pb-STI as described above. The shift in threshold energy (ΔE_0) was varied as a global parameter in the fit procedure.

3. Results and discussion

3.1 Chemical composition

The chemical composition of the produced zeolite crystals was preliminarily checked by scanning electron microscopy. EDS spectra collected on different crystal-fragments showed that Na was completely replaced by Pb. An anomalous high content of Pb was observed at all analytical points. Hence, additional chemical analyses were carried out by electron microprobe. In agreement with SEM-EDS analyses, no significant amount of calcium was detected (average CaO content less than 0.2 wt.%), indicating that the cation exchange was successful (Table 2). The elemental concentration maps indicated that Pb was homogeneously distributed in the crystals (Fig. S1). Also in this case, a high Pb content was measured at all analytical points (Table 2), resulting in a surplus of Pb species theoretically needed to balance the net negative charge of the aluminosilicate framework (13.4 instead of 8 Pb per formula

unit (pfu)) if all extraframework cations were represented by Pb^{2+} ions. Thus, none of the chemical analyses passed the balance error test ($-10\% < E < 10\%$) [43]. The surplus of EF cationic charges, referred to as overexchange process [16] was reported for other Pb-zeolites in literature [17-21] and it implies the presence of OH^- groups inside in the zeolitic channels, likely associated with the EF Pb, in order to reach charge neutrality.

Thermal gravimetric analyses showed that 9.23 wt.% was lost from the sample after a thermal treatment up to 500 °C (Fig. 1). The trend of the thermogravimetric curve indicated that H_2O is released continuously as a function of increasing temperature. Considering the loss of weight as evaporated H_2O and assuming a completely dehydrated sample at 500 °C, the water content of Pb-STI is equal to 9.23 wt.%. This is apparently in contrast with the corresponding H_2O content determined by EMPA (< 4.9 wt.%, Table 2). The EMPA analyses were done in vacuum, however, which can trigger the release of H_2O from the zeolite structure and lead to an underestimation of its content. Moreover, a Pb-STI with such low H_2O content would have a more contracted structure compared to that determined by SC-XRD, as demonstrated by the MD simulations of the second structural model PbSTI-12-2W (i.e. a Pb-STI containing 6 wt.% of H_2O) (Table S1). Thus, based on our observations, the chemical composition of Pb-exchanged stellerite can be written as: $\text{Pb}_{13.4}(\text{OH})_{10}\text{Al}_{17.4}\text{Si}_{54.6}\text{O}_{144} \cdot 38\text{H}_2\text{O}$, which corresponds to a Pb-STI with approximately 50% Pb overexchange and a water content equal to 9 wt.%.

3.2 Crystal structure

Crystal structure refinements were attempted in both $Fmmm$ and $C2/m$ space groups. The monoclinic space group $C2/m$ was previously transformed to the pseudo-orthorhombic setting $F2/m$ [44] for a better comparison with the $Fmmm$ symmetry. The cell parameters were: $a = 13.6116(5)$, $b = 18.1458(8)$, $c = 17.8234(7)$ Å, and $V = 4402.3(3)$ Å³ in space group $Fmmm$ and $a = 13.6126(3)$, $b = 18.1447(7)$, $c = 11.2134(3)$ Å, $\beta = 127.37^\circ$, and $V = 2201.12(11)$ Å³ in space group $C2/m$. Transformation to $F2/m$ using the matrix [100;0-10;-10-2] leads to lattice

parameters $a = 13.6126(3)$, $b = 18.1447(7)$, $c = 17.8231(5)$ Å, $\beta = 90.000(10)^\circ$, and $V = 4402.2(2)$ Å³. The internal agreement factors of symmetry equivalents reflections were comparable for the two systems ($R_{\text{int}} = 0.0659$ $R_{\text{sigma}} = 0.0408$ in *Fmmm*; $R_{\text{int}} = 0.0674$ $R_{\text{sigma}} = 0.0495$ in *F2/m*) as well as the R agreement factors obtained from the two structural models ($R = 0.0673$ in *Fmmm* and 0.0691 in *F2/m*). However, the following observation pointed to the orthorhombic symmetry: In **STI** framework type, the channels parallel to [100] are symmetrically equivalent in *Fmmm* (Fig. 2a) but not in *F2/m*, where they have a more elliptical shape (see for example Na-STI and CaNa-STI [25] (Fig. S2)). In the monoclinic Pb-STI structure, these two channels (I and II) are almost identical ($I = 5.62 \times 7.56$, $II = 5.62 \times 7.54$ Å) and no pronounced distortion is observed (Fig. S2). Hence, the *Fmmm* space group was preferred.

The atom parameters of Pb-STI are reported in Table 3. The aluminosilicate framework did not show significant differences from that of the natural stellerite. However, the distribution of the EF cations and H₂O completely changed. According to the chemical analyses, the extraframework species present in the Pb-STI cavities are Pb, H₂O and OH⁻ groups, which are needed to balance the Pb²⁺ surplus. Diffuse and broad electron density spread along the cavities (Fig. 2b), hampering a unique assignment of the EF cations, OH⁻ and H₂O. The modelling of the pronounced disorder resulted in several low-occupancy sites close to each other (Table 3). Crystallographic sites refined with Pb scattering factors showed maximum occupancy equal to 10 %. Six sites were attributed to H₂O and refined with oxygen scattering factors. Nevertheless, due to the strong disorder, it was difficult to unequivocally determine the coordination environment of Pb, and therefore the type of Pb-OH/H₂O interactions, based on XRD analysis.

3.3 Extraframework species and coordination chemistry of Pb²⁺

Since the determination of the local environment of the Pb species based on XRD was complicated by the pronounced structural disorder, the arrangement of the EF cations and the analysis of the coordination chemistry was based on MD simulations and XAFS results.

The average unit cell parameters obtained from MD trajectories of the PbSTI-12 model are reported in Table 4. These values are in good agreement with the experimental ones from SC-XRD. The distribution of the EF occupants within the zeolitic cavities obtained in MD simulations is disordered, confirming the experimental results from SC-XRD. The radial distribution functions (RDF) calculated for Pb-O_f (O_f = oxygen of the framework), Pb-O_w (O_w = oxygen of the H₂O) and Pb-O_h (O_h = oxygen of the OH⁻), are reported in Fig. 3a. The average bond distances are 2.30 and 2.50 Å for Pb-O_h and Pb-O_w, respectively. In contrast, the corresponding Pb-O_f curve shows that the bonding-interactions between Pb and the oxygen of the framework are unspecific and less significant compared to Pb-O_w and Pb-O_h. The average coordination of Pb can be retrieved from the running coordination number (RCN) curve reported in Fig. 3b. Each Pb is approximately coordinated by two H₂O at distances between 2.3 and 2.6 Å and by one OH⁻ group at 2.3 Å. Longer distances (mainly > 2.7 Å) are found between Pb and framework oxygen atoms.

The lack of a long-range order in the coordination shell of Pb was corroborated by EXAFS analysis. EXAFS Pb L₃-edge $k^3\chi(\kappa)$ -weighted function and its Fourier transform (FT) (not corrected for phase shift) are reported in Fig. 4a,b. The best fit was obtained by using a five-shell model (Table 5). Two Pb-O shells, Pb-O₁ and Pb-O₂, indicating a split coordination environment, were used to fit the main peak of the FT magnitude at 1.7 Å. Pb coordinates to less than one O (CN = 0.7) at 2.21 Å and to 1.42 O at 2.35 Å, corresponding to OH and OH₂ ligands. An additional Pb-O (Pb-O₃, CN = 0.5, R = 3.40 Å) and two Pb-Si (Pb-Si₁ and Pb-Si₂) shells fitted the spectral features in the region between 2.8 and 4.3 Å, and correspond to atoms of the zeolite framework. According to the calculated running coordination number (Fig. 3b),

Pb-O distances at 2.20 Å occur mainly between Pb and OH⁻ groups. The second shell Pb-O₂ is attributed to Pb-OH⁻ and Pb-H₂O bonds. Pb-Si distances and coordination numbers of Pb-Si₁ and Pb-Si₂ shells match with the theoretical values reported in Fig. 3b (keeping in mind that due to similar electron density, Si and Al cannot be distinguished by EXAFS). The interpretation of the Pb-O₃ shell is less obvious. Longer Pb-O distances are found between Pb and OH⁻, H₂O and framework oxygen. However, according to RCN calculated from MD simulations, a low coordination number (CN = 0.5) at such long distances (3.4 Å) agrees, also in this case, with Pb-OH⁻ interactions (Fig. 3b). The obtained experimental spectrum fairly well agrees with the theoretical spectrum obtained from the MD trajectories (Fig. 4c). Small deviation of the theoretical $k^3\chi(\kappa)$ -function from the experimental one, could be related to slight differences between the real chemical-composition of the sample and the idealized MD model.

Thus, according to experimental and theoretical data, the first coordination shell of Pb²⁺ is constituted by OH⁻ and H₂O. The average <Pb-O_w> distance is in agreement with that expected from the sum of atomic radii (ca. 2.52 Å) whereas the <Pb-O_h> distance is significantly smaller. Short Pb-O distances, in the range of 2.2 and 2.3 Å, were reported for other Pb-silicate structures [45,46] where Pb adopts a distorted coordination due to the stereochemical activity of the lone pair electrons. A similar configuration was also observed in our theoretical structure: Each *t-sti-1** cavity hosts one Pb atom, which is mainly surrounded by H₂O, or two Pb atoms coordinated by OH⁻, H₂O and (at longer distances) by framework O (Fig. 5a). In the first case, the arrangement of Pb resembles that of Ca in natural stellerite, that is Pb is coordinated by 5 or 6 H₂O (Fig. 5b). Alternatively, when Pb₂(OH)₂ species are present (i.e. more than one Pb atom per cavity) Pb atoms show a sided coordination with OH⁻ groups (at short distances < 2.3 Å) and H₂O, and longer contacts (> 2.8 Å) with the oxygen of the aluminosilicate framework (Fig. 5c).

Recently, the presence of Pb-Pb clusters was reported for Linde Type A (LTA) zeolite exchanged with Pb [15]. Such clusters were characterized by unusual Pb-Pb short distances (2.90 Å) and were reported to occur in the hydrated as well as in the dehydrated structure of Pb-LTA. In our study, we do not have evidence of Pb-clusters. The shortest Pb-Pb distance, estimated from the calculated structure, is 3.5 Å. Further, none of the peaks in the FTM range of the experimental EXAFS spectrum had the characteristics of a heavy backscatterer like Pb as checked by wavelet transform analysis [47].

3.4 Framework modification and comparison with other metal-exchanged STI forms

Pb-STI maintains the *Fmmm* space group of natural stellerite (Ca-STI) without evident changes in the framework topology. This is in contrast with the trend observed in the other forms of stellerite (Na-STI, Ag-STI, Cd-STI [27]) where the symmetry is lowered to monoclinic and an increased degree of distortion (in terms of the beta monoclinic angle and elliptical shape of the channels) is observed. It is worth noting, that a structural strain/distortion at RT may play a role in the dehydration path and subsequent thermal behaviour of cation-modified zeolites upon heating [26-27]. To quantify the degree of framework distortion, we refer to the L/S ratio of the channels, as defined by Bauer and Baur [48]. This is the ratio between the distance of the opposite oxygen sites along the longest L and shortest S diagonals. The L/S ratios for the known exchanged forms of stellerite are reported in Table 6. The L/S values of Pb- and Ca-STI are, as expected, equal, being the size of the channels of Pb-STI (5.61×7.54 Å) almost the same of that of Ca-STI (5.64×7.55 Å). Cd-STI is the zeolite with the most elliptical channels, and, compared to Ag- and Na-STI, it is also the one with the lowest thermal stability. Based on these results, we expect that the thermal stability of Pb-STI may be similar to that of Ca-STI, or at least higher than that of Ag- and Cd-STI.

The disorder of the EF species was observed in all exchanged forms of **STI** framework type zeolites. Nevertheless, in Pb-STI disorder is significantly more pronounced compared to Na-,

Ag- and Cd-STI. In Pb-STI, several local configurations, which differ from each other, arise as a consequence of the overexchange (and therefore of the presence of OH⁻ groups) and lead to the lack of a long-range periodicity of the EF occupants.

4. Conclusions

Our data unequivocally showed that an overexchange of approximately 50% of Pb occurred during the experiments in aqueous solution. The degree of this overexchange has been related to the pH, and therefore to the available aqueous species, of the solution [17]. Our experimental conditions (pH and molarity of the solution) were similar to those applied in other studies [19,20,21] where a surplus of Pb in zeolitic structures was observed. Thus, the 50% excess of Pb is plausible.

Detailed knowledge and the control of EF-cations speciation is essential for the assessment of potential properties of the ion-exchanged zeolites and thus their practical applications. This kind of investigation can be, and it is in most heavy-metal exchanged zeolites, complicated by the structural disorder, eventual presence of more than one oxidation state of the EF cations, and formation of several type of EF species, including metal clusters. For this reason, although XRD still represents one of the most appropriate technique to investigate the structural features of porous materials, an accurate characterization of framework-EF interactions requires complementary methods. In this study, by combining theoretical calculations, SC-XRD and XAFS experiments, we could unravel the distribution of the extraframework occupants and the coordination chemistry of Pb²⁺: each *t-sti-I** cavity contains either one Pb²⁺, mainly coordinated by H₂O, or two Pb²⁺, coordinated to OH⁻ groups, H₂O molecules and oxygen atoms of the framework. On average, Pb²⁺ is coordinated by 0.8 O (belonging to OH⁻ groups) at short distances (~2.2 Å) and by 1.3 O (belonging to H₂O or OH⁻) at 2.36 Å in its first coordination shell, while bonding interactions between Pb²⁺ and oxygen of the framework

occur only at larger distances ($>2.7 \text{ \AA}$). XAFS experiments indicated that Pb-clusters, as found in LTA zeolite [15], do not occur in the hydrated form of Pb-STI.

The performed analysis indicates that the uptake of Pb^{2+} into **STI** framework does not induce structural strain on the framework that has been revealed in the previous studies for Cd- and Ag-STI [27]. The orthorhombic symmetry with space group *Fmmm* of natural stellerite (Ca-STI) is preserved after the Pb-exchange. Based on these findings, we speculate that the thermal stability of Pb-STI could be higher with respect to that of Ag- and Cd-STI. In this case, it would be interesting to figure out i) how the Pb-overexchange influences the dehydration of Pb-STI; ii) how the different Pb-species evolve upon heating; and iii) which kind of structural topologies will form. For this reason, a study on the structural changes occurring in Pb-STI at high temperatures is currently in progress.

Acknowledgements

We are thankful to Thomas Armbruster who reads the final version of the manuscript. We acknowledge access to the Swiss National Supercomputing Center (CSCS) and UBELIX HPC cluster at the University of Bern.

Funding

The Swiss National Science Foundation (SNF) is acknowledged for the Ambizione grant n. PZ00P2 173997 awarded to G. C.

References

[1] C. Colella, Environmental applications of natural zeolitic materials based on their ion-exchange properties. In: Application of natural microporous materials in environmental technology; Misaelides, P., Macasek, F., Pinnavaia, T. J. Colella, C. Eds.; NATO Science Series (Applied Sciences); Kluwer:Dordrecht, 1999, Vol. E362.

- [2] S. Wang, Y. Peng, *Chem. Eng. J.* 156 (2010) 11-24.
- [3] M. Ackley, S. U. Rege, H. Saxena, *Microporous Mesoporous Mater.* 61 (2003) 25-42.
- [4] X. Chen, B. Shen, H. Sun, G. Zhan, *Microporous Mesoporous Mater.* 261 (2018) 227-236.
- [5] P. Aprea, B. De Gennaro, N. Gargiulo, A. Peluso, B. Liguori, F. Iucolano, D. Caputo, *Appl. Therm. Eng.* 106 (2016) 1217-1224.
- [6] S. S. Arzumanov, A. A. Gabreinko, A. V. Toktarev, Z. N. Lashchinskaya, D. Freude, J. Haase, A. G. Stepanov, *J. Phys. Chem. C* 123 (2019) 30473–30485.
- [7] Y. Zhang, Y. Qu, D. Wang, X. C. Zeng, J. Wang, *Ind. Eng. Chem. Res.* 2017, 56, 12508-12519.
- [8] N. Abreu, H. Valdes, A. C. Zaror, F. Azzolina-Jury, M. Melendrez, *Microporous Mesoporous Mater.* 274 (2019) 134-148.
- [9] J. Milenkovic, J. Hrenovic, D. Matijasevic, M. Niksic, N. Rajic, *Environ. Sci. Pollut. Res.* 24 (2017) 20273-20281.
- [10] P. Granger, V. I. Parvulescu, *Chem. Rev.* 111 (2011) 3155-3207.
- [11] J. Perez-Pellitero, G. D. Pirngruber. *Industrial Zeolite Applications for Gas Adsorption and Separation Processes*. In: S. Valencia, F. Rey Eds. *New Developments in Adsorption/Separation of Small Molecules by Zeolites. Structure and Bonding*, vol 184. Springer, Cham.
- [12] I. Sökmen, F. Sevin, *J. Colloid Interface Sci.* 264 (2003) 208-211.
- [13] S. Chibani, I. Medlej, S. Lebègue, J. G. Angyan, L. Cantrel, M. Badawi, *Chem. Phys. Chem.* 18 (2017) 1642-1652.
- [14] A. Thanos, E. Katsou, S. Malamis, V. Drakopoulos, P. Paschalakis, E. A. Pavlatou, K. J. Haralambous, *Appl. Clay Sci.* 147 (2017) 54-62.

- [15] W. Baekelant, S. Aghakhani, E. Coutino-Gonzalez, D. Grandjean, K. Kennes, D. Jonckheere, E. Fron, F. D'Acapito, A. Longo, P. Lievens, M. B. J. Roeffaers, J. Hofkens, J. Phys. Chem. C 2018, 122, 13953-13961.
- [16] E. Hertzberg, H. Sherry, ACS Symp Ser. 135 (1980) 187.
- [17] C. Ronay, K. Seff, J. Phys. Chem. 89 (1985) 1965-1970.
- [18] C. Ronay, K. Seff, Zeolites 13 (1993) 97.
- [19] Y. H. Yeom, Y. Kim, K. Seff, J Phys Chem B 101 (1997) 5314-5318.
- [20] G. Nardin, L. Randaccio, E. Zangrando, Zeolites 15 (1995) 684-688.
- [21] W. Shibata, K. Seff, Zeolites 19 (1997) 87-89.
- [22] E. Galli, Alberti, A. Bull. Soc. Fr. Mineral. Cristallogr. 98 (1975) 11-18.
- [23] C. Baerlocher, W. M. Meier, D. H. Olson. Atlas of Zeolites Framework Types, Structure Commission of the IZA, 5th ed. Elsevier, 2001.
- [24] R. Arletti, E. Mazzucato, G. Vezzalini, Am. Mineral. 91 (2006) 628-634.
- [25] G. Cametti, M. Fisch, T. Armbruster, Microporous Mesoporous Material. 253 (2017) 239-250.
- [26] G. Cametti, A. C. Scheinost, M. Giordani, S. V. Churakov, J. Phys. Chem. C 123 (2019) 13651-13663.
- [27] G. Cametti, A. C. Scheinost, S. V. Churakov, J. Phys. Chem. C 123 (2019) 25236-25245.
- [28] J.V. Smith, Chem. Rev. 88 (1988) 149-182.
- [29] T. Armbruster, T. Kohler, T. Meisel, T. F. Nägler, M. A. Götzinger, H. A. Stadler, Mineral. Petrogr. Mittl. 76 (1996) 131-146.
- [30] APEX3, v2018.7-2; Bruker, AXS, 2017.
- [31] G. M. Sheldrick, Acta Crystallogr. A 64 (2008) 112-122.
- [32] G. M. Sheldrick, Acta Crystallogr. C 71 (2015) 3-8.
- [33] K. Momma, F. Izumi, J. Appl. Crystallogr. 44 (2011) 1272-1276.

- [34] T. Kühne, M. Iannuzzi, M. Del Ben, V. Rybkin, P. Seewald, et al. *J. Chem. Phys.* 152 (2020) 194103.
- [35] J. P. Perdew, K. Burke, M. Ernzerhof, *Phys. Rev. Lett.* 77 (1996) 3865-3868.
- [36] J. VandeVondele, J. Hutter, *J. Chem. Phys.* 127 (2007) 114105.
- [37] S. Grimme, *J. Comput. Chem.* 27 (2006) 1787-1799.
- [38] A. L. Ankudinov, B. Ravel, J.J. Rehr, S. D. Conradson, *Phys. Rev. B* 58 (1998) 7565-7576.
- [39] A. L. Ankudinov, J. J. Rehr, *Phys. Rev. B* 62 (2000) 2437-2445.
- [40] A. C. Scheinost, J. Claussner, J. Exner, M. Feig, S. Findeisen, C. Hennig, K. O. Kvashnina, D. Naudet, D. Prieur, A. Rossberg, M. Schmidt, C. Qiu, P. Colomp, C. Cohen, E. Dettona, V. Dyadkin, T. Stumpf, *J. Synchrotron Rad.* 28 (2021) 333-349.
- [41] T. Ressler, *J. Synchrotron Radiation* 5 (1998) 118-122.
- [42] A. L. Akudinov, J. J. Rehr. *Phys. Rev. B* 56 (1997) R1712-R1715
- [43] E. Passaglia, *Am. Mineral.* 55 (1970) 1278-1301.
- [44] S. Quartieri, G. Vezzalini, *Zeolites* 7 (1987) 163-170.
- [45] U. Kolitsch, D. Holtstam, *Mineralogical Magazine* 66 (2002) 353-363.
- [46] A. R. Kampf, G. R. Rossman, R. M. Housley, *American Mineralogist* 94 (2009) 1198-1204.
- [47] H. Funke, A. C. Scheinost, M. Chukalina, *Physical Review B* 71 (2005) 094110.
- [48] T. Bauer, W. H. Baur, *Eur. J. Miner.* 10 (1998)133.

Tables

Table 1 Crystal data and refinement parameters of Pb-STI

Crystal data	Pb-STI
a (Å)	13.6116(5)
b (Å)	18.1458(8)
c (Å)	17.8234(7)
V (Å ³)	4402.3(3)
Z	1
Space Group	$Fmmm$
Refined Chemical formula	$\text{Pb}_{12}(\text{OH})_8(\text{Si},\text{Al})_{72}\text{O}_{144} \cdot 58\text{H}_2\text{O}$
Crystal size (mm)	$0.07 \times 0.100 \times 0.200$
Intensity measurement	
Diffractometer	Bruker Apex II
X-ray radiation	$\text{MoK}\alpha$ $\lambda = 0.71073$ Å
X-ray power	50 kV, 60 mA
Monochromator	Graphite
Temperature (°C)	25
Exposure time (s)	10
Max. 2θ (°)	53.16
Index ranges	$-16 \leq h \leq 17$ $-22 \leq k \leq 22$ $-22 \leq l \leq 21$
No. of measured reflections	13853
No. of unique reflections	1279
No. of observed reflections $I > 2\sigma(I)$	999
Structure refinement	
No. of parameters used in the refinement	131
$R(\text{int})$	0.0659
$R(\sigma)$	0.0408
GooF	1.075
$R1, I > 2\sigma(I)$	0.0673
$R1, \text{all data}$	0.0852
$wR2$ (on F^2)	0.1886
$\Delta\rho_{\text{min}}$ ($-\text{e}\text{\AA}^{-3}$) close to	-1.11 W2
$\Delta\rho_{\text{max}}$ ($\text{e}\text{\AA}^{-3}$) close to	0.93 C3A

Table 2 Quantitative chemical analyses of Pb-STI obtained from EMPA

Average composition of 27 point analyses				min.	max.	St.Dev.
	wt.-%		p.f.u. ^b	p.f.u. ^b	p.f.u. ^b	
SiO ₂	43.48	Si	54.62	53.93	55.15	0.04
Al ₂ O ₃	11.74	Al	17.38	16.85	18.06	0.04
FeO	0.07	Fe	0.07	0	0.31	0.01
MnO	0.08	Mn	0.09	0	0.34	0.01
MgO	0.00	Mg	0.00	0	0.08	0.002
CaO	0.18	Ca	0.24	0	0.46	0.01
SrO	0.00	Sr	0.00	0	0	0
BaO	0.07	Ba	0.04	0	0.31	0.01
Na ₂ O	0.02	Na	0.06	0	0.23	0.01
K ₂ O	0.03	K	0.05	0	0.12	0.005
PbO	39.42	Pb	13.38	10.96	15.28	0.17
Total	95.10	OH ⁻ ^c	10.75	5.92	14.6	
H ₂ O + OH ⁻ ^a	4.90	H ₂ O	14.94	6.63	27.5	0.64
		E%	-36.81	-45.89	-26.23	

^a H₂O + OH⁻ in wt.-% calculated as difference to 100%.

^b Atoms per formula unit calculated on the basis of 72 (Si + Al).

^c Estimated OH⁻ p.f.u. based on charge balancing Pb-overexchange.

Table 3 Atom coordinates, occupancy and atomic displacement parameters of Pb-

STI

Site	Scattering factors	x	y	z	Occ.	U ^{eq}
T1	Si	0.11129(15)	-0.18342(12)	0.5	1	0.0166(5)
T2	Si	0.11389(11)	-0.30729(8)	0.62366(9)	1	0.0177(4)
T3	Si	0.25	-0.25	0.75	1	0.0209(7)
T4	Si	0.30114(16)	-0.08896(12)	0.5	1	0.0196(5)
O1	O	0	-0.3167(4)	0.6518(4)	1	0.0357(16)
O2	O	0.3072(7)	0	0.5	1	0.032(2)
O3	O	0.1269(3)	-0.2321(3)	0.5751(3)	1	0.0357(12)
O4	O	0.1824(3)	-0.3040(3)	0.6991(3)	1	0.0351(12)

O5	O	0.1849(5)	-0.1129(4)	0.5	1	0.0366(17)
O6	O	0.1443(4)	-0.3803(3)	0.5754(3)	1	0.0418(13)
O7	O	0	-0.1486(5)	0.5	1	0.0270(19)
C1	Pb	0.25	-0.4506(2)	0.75	0.154(4)	0.099(3)
C2	Pb	0	-0.5	0.6113(6)	0.147(7)	0.076(3)
C2A	Pb	0	-0.5	0.6475(14)	0.067(8)	0.048(7)
C2B	Pb	0.052(3)	-0.5	0.6560(18)	0.027(4)	0.075(13)
C3	Pb	0.3055(9)	-0.4301(4)	0.6986(4)	0.081(4)	0.067(3)
C3A	Pb	0.3483(9)	-0.4337(4)	0.6869(4)	0.095(4)	0.080(3)
C3B	Pb	0.355(3)	-0.473(2)	0.653(3)	0.0122(13)	0.08
C4	Pb	0.0550(6)	0	0.4811(7)	0.060(4)	0.037(4)
C4A	O	0.075(5)	0	0.778(4)	0.14(2)	0.06
C4B	Pb	0	0	0.4726(13)	0.037(5)	0.064(11)
C5	Pb	0	0	0.709(4)	0.013(2)	0.06
W1	O	0.5	-0.3845(6)	0.7022(6)	1	0.056(3)
W1A	O	0.4514(13)	-0.3874(10)	0.6907(10)	0.52(2)	0.084(7)
W2	O	0.1345(17)	-0.5	0.6912(12)	1	0.15
W3	O	0.0672(12)	0	0.4481(16)	0.59(5)	0.040(5)
W3A	O	0.088(3)	0	0.394(2)	0.26(2)	0.06
W3B	O	0	0	0.407(4)	0.21(3)	0.06

Table 4 Unit cell parameters of Pb-STI obtained from MD trajectories and SC-XRD.

The difference between theoretical and experimental results is reported in percentage

	MD	XRD	Deviation(%)
<i>a</i> -axis (Å)	13.557	13.6116(5)	0.40
<i>b</i> -axis (Å)	18.209	18.1458(8)	0.34
<i>c</i> -axis (Å)	17.726	17.8234(7)	0.54
α (°)	89.25	90	0.82
β (°)	89.04	90	1.06
γ (°)	90.17	90	0.19
Cell volume (Å ³)	4375.26	4402.3(3)	0.61

Table 5 Structural parameters of Pb-STI determined from EXAFS analysis

Shell	CN $\pm 25\%$	R(\AA) ± 0.01	σ^2 (\AA^2) ± 0.002
Pb-O ₁	0.8	2.20	0.005 ^a
Pb-O ₂	1.3	2.36	0.005 ^a
Pb-O ₃	0.5	3.40	0.005 ^a
Pb-Si ₁	1.1	4.06	0.01 ^b
Pb-Si ₂	1.2	4.35	0.01 ^b
ΔE_0 (eV)		-4.76	
χ -residual		6.5	
^{a,b} constrained to be equal			
CN: Coordination Number			
R: Absorber-scatterer distance			
σ^2 : Debye-Waller factor			

Table 6 L/S Ratio [48] of the ten-membered ring channels (I and II) in the different cationic forms of **STI** zeolite. Channel I and II are equivalent for symmetry in Ca- and Pb-STI

Zeolite	Space Group	L/S I	L/S II
Ca-STI	<i>Fmmm</i>	1.34	1.34
Na-STI	<i>F2/m</i>	1.36	1.33
Ag-STI	<i>F2/m</i>	1.40	1.28
Cd-STI	<i>F2/m</i>	1.48	1.29
Pb-STI	<i>Fmmm</i>	1.34	1.34

Figure Captions

Figure 1 Thermogravimetric curve of Pb-STI from 25 to 500°C.

Figure 2 Ball –and-stick representation of Pb-STI framework. (a) Size of the channels parallel to [100] (in Å) and (b) isosurfaces of the electron density corresponding to the EF species (isosurfaces level $>1.9 \text{ e}^-/\text{Å}^3$). Channel I and II are equivalent for symmetry.

Figure 3 Radial Distribution Function (RDF) (a) and Running Coordination Number (RCN) (b) of Pb-O_f, Pb-O_w, Pb-O_h, Pb-Si, and Pb-Al in Pb-STI structure obtained from MD trajectories. O_f, O_w, and O_h refer to framework, H₂O and OH⁻ oxygen, respectively.

Figure 4 (a) L₃-edge $k^3\chi(\kappa)$ -weighted function and corresponding (b) Fourier-transformed EXAFS (uncorrected for phase shift) of Pb-STI. Blue circles and red line represent the experimental data and the fitting, respectively. Measured (dashed line) and fitted (continuous line) imaginary part of the FT are also shown. (c) Comparison between the experimental and theoretical $k^3\chi(\kappa)$ -weighted function calculated from MD trajectories.

Figure 5 (a) Representative snapshot from MD trajectories showing the distribution of Pb, H₂O, and OH⁻ within adjacent cages parallel to [100] in Pb-STI structure. Blue and red sticks represent the framework. Dark grey, red and white spheres correspond to Pb, O, and H, respectively. (b,c) Possible local environment of Pb atoms in two adjacent cages.

Figures

Figure 1

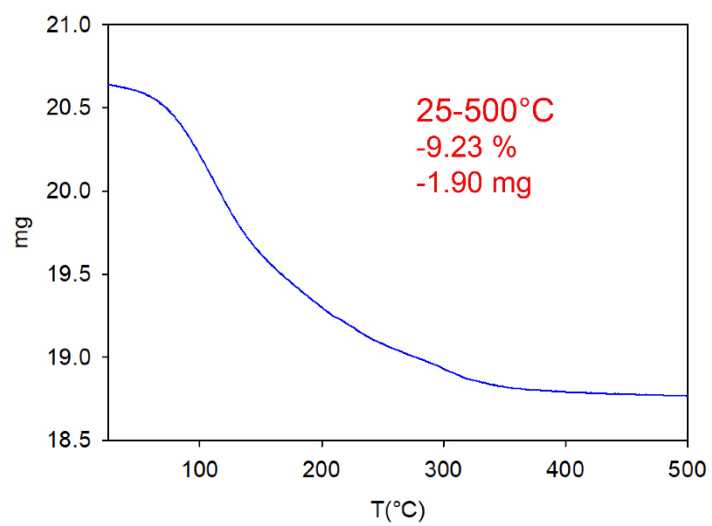


Figure 2

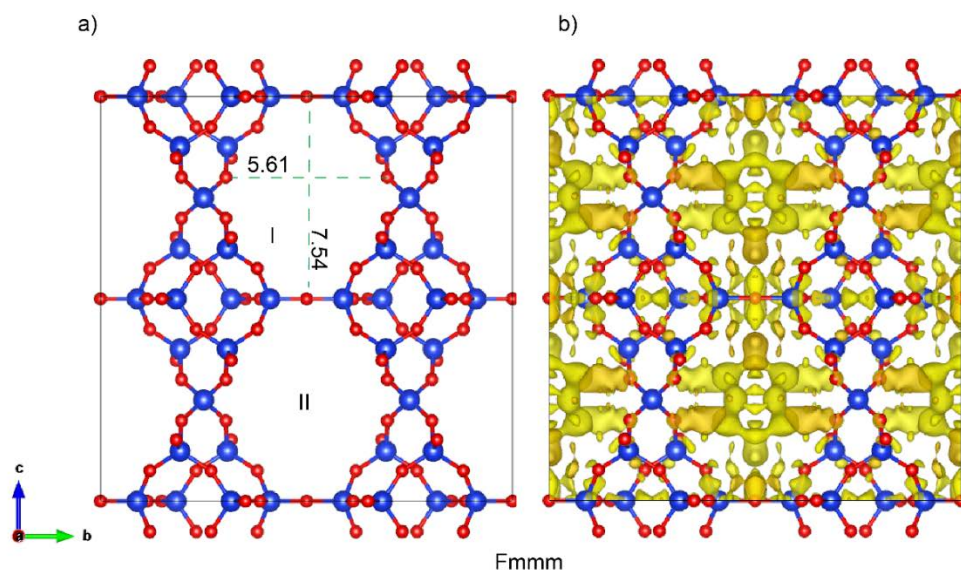


Figure 3

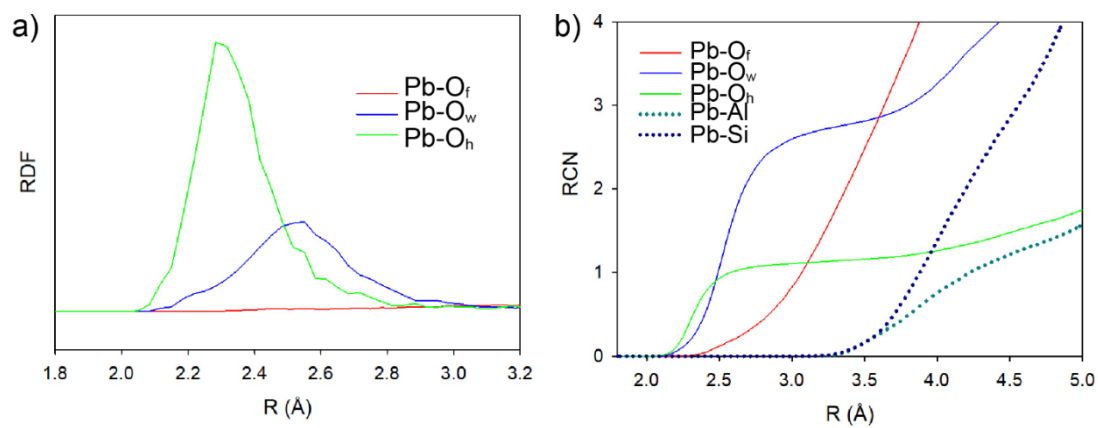


Figure 4

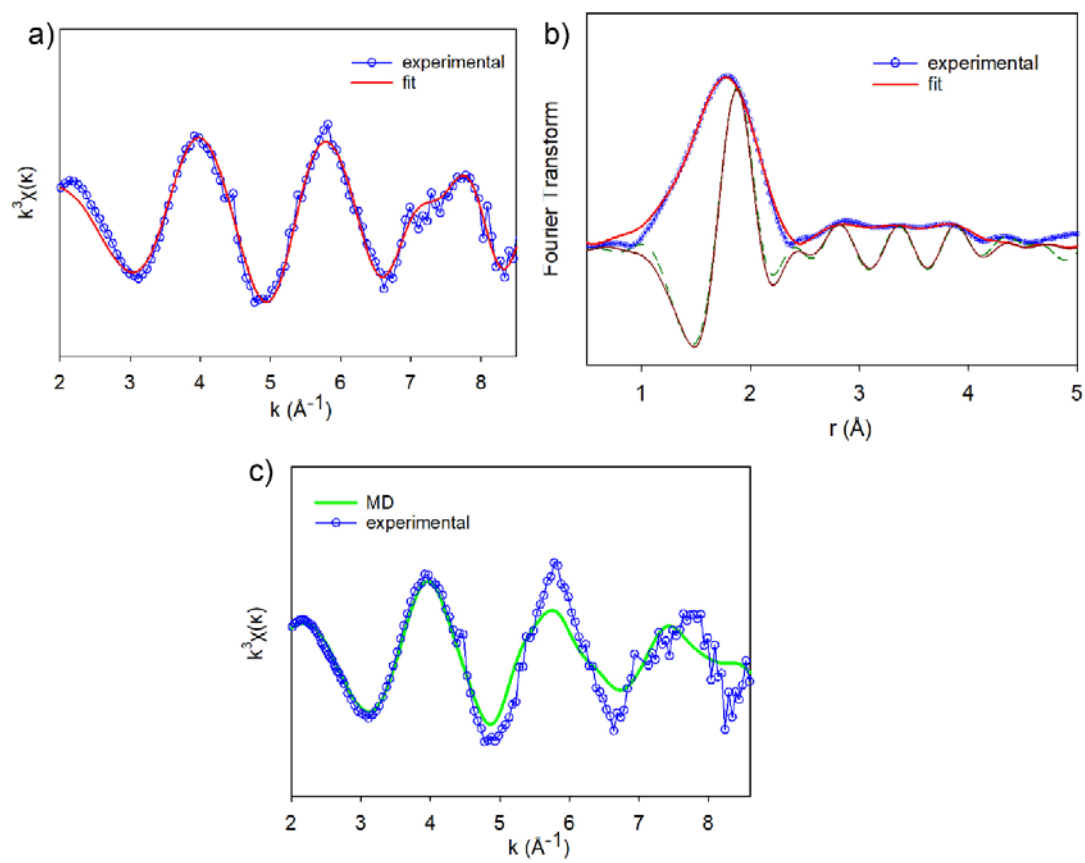


Figure 5

